Electronic states in a cylindrical quantum lens: Quantum chaos for decreasing system symmetry

C. Trallero-Herrero,[1] C. Trallero-Giner,[2] S. E. Ulloa,[3] and R. Perez-Alvarez[2]
[1]*Nuclear Physics Department, Higher Institute for Nuclear Science and Technologies, Avenida Salvador Allende y Luaces, Vedado, Havana, Cuba*
[2]*Department of Theoretical Physics, Havana University, 10400, Havana, Cuba*
[3]*Department of Physics and Astronomy and CMSS Program, Ohio University, Athens, Ohio 45701-2979*
(Received 3 April 2001; revised manuscript received 16 July 2001; published 30 October 2001)

The eigenvalue problem in a cylindrical lens geometry is studied. Using a conformal mapping method, the shape of the boundary and the Hamiltonian for a free particle are reduced to those of a two-dimensional problem with circular symmetry. The wave functions are separated into two independent Hilbert subspaces due to the inherent symmetry of the problem. For small geometry deformations, the solutions are found by a specially designed perturbation approach. Comparisons between exact and perturbative solutions are made for different lens parameters. As the symmetry of the lens is reduced, the characteristics of the spectrum and the corresponding spatial properties of the wave functions are studied. Our results provide a family of billiard geometries in which the electronic level spectrum is well characterized. In analyzing the level spacing distribution of the spectrum, a strong deviation from the Poisson and Wigner limiting distributions is found as the boundary geometry changes. This intermediate distribution is indicative of a mixed phase space, also revealed explicitly in the classical Poincaré maps we present.

DOI: 10.1103/PhysRevE.64.056237 PACS number(s): 05.45.Mt, 73.21.−b, 03.65.Ge, 78.30.Fs

I. INTRODUCTION

Advances in materials fabrication and lithographic techniques have given us a variety of experimental systems where electronic properties are tested in different environments. Notable among these are the ''quantum dots'' which confine electrons to dimensions comparable to their characteristic wavelength [1,2]. Different approaches produce fully confined electronic systems with a discrete energy spectrum, as well as quantum-wire-like geometries which have a continuum component in one direction (but discrete otherwise on the plane perpendicular to the given direction) [3]. Similarly, effectively two-dimensional systems are produced in semiconductor heterojunctions, where electrons are strongly confined to a plane, while other potentials restrict their motion on the plane to a region with finite size and definite shape. A number of micrometer and submicrometer two-dimensional ''stadia'' have been studied as prototypes of interesting electronic dynamical systems that reflect regular and chaotic dynamics, depending on the specific boundary geometry [4,5]. The associated level spectra of these systems have been shown to exhibit characteristic features reflecting the different degrees of integrability of the classical system (see Ref. [6] and references therein).

Furthermore, as electronic transport and optical properties are determined by the details of the energy spectrum, it is important to know precisely the effects of geometrical confinement on the electronic states. Simple geometries with well-known spectra are few, while realistic systems with complex shapes are not as well characterized. In this work, we undertake the study of a set of circular cap lens geometries that can be manufactured by a variety of different approaches. It is particularly important that our method allows the study of the corresponding spectrum as a function of how ''flat'' the circular cap lens is (i.e., the ratio of the radius to the height of the lens). This study represents then a family of shapes with well-characterized level spectra and properties.

Another goal of the present paper is to study the appearance of chaos in a cylindrical quantum lens in terms of its geometric parameters, by studying the details of the level spectrum spacings. We follow the general trends concerning the anticrossing between nearby energetic levels with the same symmetry, the increasing number of repulsion levels when the problem transits from an integrable system to a chaotic one, and how for a small geometric perturbation the states can be well described by perturbation theory. We find that, as the lens becomes flatter, the energy level spacing distribution reflects a transition from a purely ''integrable'' system, described by a Poisson distribution function, to one that exhibits chaotic dynamics, and that, for large deformations of the semispherical (-circular) cap, the level statistics reflects the complex character of a mixed phase space. In what follows, we describe the geometry of an effectively two-dimensional spectrum, either because the confinement in the third direction is so extreme that its dynamics is ''frozen'' [4,5], or because the system is a long cylindrical lens-shaped ''wire'' [3], and thus has a continuous spectrum along the long direction (and a discrete two-dimensional manifold along the orthogonal plane).

The paper is organized as follows. Section II is devoted to presenting the cylindrical quantum lens geometry and the conformal transformation mapping method valid for this problem. In Sec. III, we describe our approach to obtaining the level spectrum and corresponding eigenfunctions, both by perturbation theory and by direct solution of the Schrödinger equation. Also, we analyze the chaotic behavior through the level spacing distribution and the lens geometry, and correlate this behavior with Poincaré surfaces of section of the corresponding classical system. Finally, in Sec. IV, we discuss the consequences of this work.

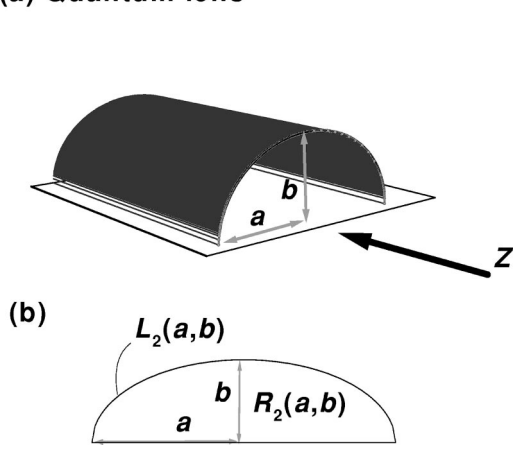

FIG. 1. (a) System with cylindrical lens shape geometry with height b and width $2a$. (b) Two-dimensional lens domain $R_2(a,b)$ with boundary $L_2(a,b)$.

II. CYLINDRICAL QUANTUM LENS

As described in the Introduction, a typical wirelike device produced in experiments is shown in Fig. 1(a). The domain of the system in $\mathbf{r}$ space is given by an infinite cylinder with cross sectional lens shape given by a height b and width $2a$, as indicated. The states of a free carrier inside such devices are described by the stationary Schrödinger equation

$$\{\nabla_{\mathbf{r}}^2+k^2\}\psi(\mathbf{r})=0, \quad \mathbf{r}\in R_3(a,b), \tag{1}$$

where $R_3(a,b)$ denotes the domain with boundary $L_3(a,b)$ obeying the boundary condition $\psi=0$ for $\mathbf{r}\in L_3(a,b)$, and $k^2=2mE/\hbar$, where E is the energy and m is the carrier effective mass. Taking advantage of the cylindrical symmetry, solutions of Eq. (1) can be cast as

$$\psi(\mathbf{r})=f(\boldsymbol{\rho})e^{ik_z z}, \tag{2}$$

where $\boldsymbol{\rho}$ is a two-dimensional (2D) vector and k_z is the wave vector component along the z direction. Using the above solution, Eq. (1) becomes

$$\{\nabla_{\boldsymbol{\rho}}^2+\overline{k^2}\}f(\boldsymbol{\rho})=0, \quad \boldsymbol{\rho}\in R_2(a,b), \tag{3}$$

where $\overline{k^2}=k^2-k_z^2$ is the corresponding eigenvalue for $f(\boldsymbol{\rho})$ in the 2D domain $R_2(a,b)$ with boundary $L_2(a,b)$ [see Fig. 1(b)]. Solving Eq. (3) for such a 2D lens is clearly equivalent to the solution of Eq. (1) because of Eq. (2). We should also notice that solutions of Eq. (3) yield the *entire* level spectrum for a purely *two-dimensional system*, or one where the z-axis confinement is so extreme that that degree of freedom is effectively *frozen.*

For the particular case $b=a$, Eq. (3) presents exact analytical solutions due to the semicircular symmetry. Here, the boundary problem in Eq. (3) is reduced to the conditions $f(a,\theta)=0$, $f(\rho,\pi)=0$, and $f(\rho,0)=0$. The functions $f(\boldsymbol{\rho})$ in polar coordinates are given by products of integer-order Bessel functions and sine functions,

$$f_{n,p}^0(\rho,\theta)=\frac{1}{A_{n,p}}J_n\left(\frac{\mu_p^{(n)}}{a}\rho\right)\sin(n\theta), \tag{4}$$

with $n=1,2,\ldots$, $p=1,2,\ldots$, where $\mu_p^{(n)}$ is the pth zero of the Bessel function of order n. The normalization constant $A_{n,p}$ is given by

$$A_{n,p}=\frac{a\sqrt{\pi}}{\sqrt{2}}|J_{n+1}(\mu_p^{(n)})|, \tag{5}$$

and the eigenvalues $E_{n,p}=\hbar^2(\mu_p^{(n)})^2/(2ma^2)$.

The 2D quantum lens shape corresponds to the more general case when $b<a$. Here, we need to fulfill Eq. (3) with the condition $\psi=0$ over the boundary $L_2(a,b)$ (Dirichlet condition). As this problem does not present a semicircular geometry, the wave functions $f_{n,p}^0$ given by Eq. (4) are no longer the eigensolutions for this problem. To provide an analytical solution, we will use a conformal mapping transform method for partial differential equations [7]. It is convenient to perform a conformal mapping to a circular domain $R_2(a,a)$ with boundary $L_2(a,a)$ where the set $\{f_{n,p}^0\}$ of eigenfunctions (4) forms an orthonormal basis on this domain. Hence, the mapping will enable us to solve the problem in a Hilbert space where an orthonormal basis $\{f_{n,p}^0\}$ is known. We transform the 2D quantum lens domain and its boundary into a semicircular shape, so that the lens defined by the domain $\mathcal{Z}=x-iz\in R_2(a,b)$ transforms into the semicircular domain $\mathcal{W}=u-iv\in R_2(a,a)$. This is accomplished by the transformation

$$\mathcal{W}(\mathcal{Z})=\frac{2a}{1+[(a-\mathcal{Z})/a+\mathcal{Z}]^{\alpha}}-a, \quad \alpha=\frac{\pi/4}{\arctan(b/a)}, \tag{6}$$

in the $\mathcal{W}$ domain, with the parameter equations $u=\rho\sin\theta$, $v=\rho\cos\theta$, $0<\rho<a$, and $0<\theta<\pi$. Using Eq. (6) the eigenvalue problem (3) is transformed into,

$$\nabla_{(u,v)}^2F(u,v)+\mathcal{J}_{\alpha}(u,v)\overline{k^2}F(u,v)=0, \quad (u,v)\in R_2(a,a), \tag{7}$$

with boundary condition

$$F(u,v)|_{(u,v)\in L_2(a,a)}=0. \tag{8}$$

$\mathcal{J}_{\alpha}(u,v)$ is the Jacobian of the transformation $\mathcal{W}(\mathcal{Z})$, given by

$$\mathcal{J}_{\alpha}(r,\theta)=\frac{16(1/\alpha)^2}{R^{1-1/\alpha}[f_+^{1/\alpha}+f_-^{1/\alpha}+2R^{1/2\alpha}\cos(\phi/\alpha)]^2}, \tag{9}$$

with the definitions

$$r=\rho/a, \quad f_{\pm}=1+r^2\pm 2r\sin\theta, \quad R=f_+f_-, \tag{10}$$

and

$$\phi=\begin{cases}\arctan\left(\dfrac{2r\cos\theta}{1-r^2}\right), & r<1\\ \pi/2, & r=1.\end{cases} \tag{11}$$

The function $\mathcal{J}_{\alpha}(u,v)$ contains the information about the lens geometry, and it should be noted that $\alpha\geqslant 1$, since $b\leqslant a$. For $\alpha=1$, $\mathcal{J}_{\alpha}$ reduces to 1, as one would expect.

The space of solutions where Eq. (7) is defined must fulfill the boundary condition (8). Hence, the functions $F(u,v)$ for a given k_z can be expanded in term of the set $\{f^0_{n,p}\}$ such that

$$F_l = \sum_{n,p} C^{(l)}_{n,p} f^0_{n,p}(\boldsymbol{\rho}), \tag{12}$$

where $\boldsymbol{\rho}=(\rho,\theta)$ is the polar parametrization of (u,v), as described above, and l is a generic label for the new eigenstates of Eq. (7), which is related to the (n,p) indices by numbering the ordered Bessel zeros $\mu^{(n)}_p$, or energy levels, for the case of $a=b$.

It can be shown that the functions F_l form a complete set of orthonormal functions $\{F_l\}$ with weighting factor $\mathcal{J}_\alpha(\rho,\theta)$, fulfilling the condition [8]

$$\int_{R_2(a,a)} \mathcal{J}_\alpha F^*_{l'} F_l d^2\boldsymbol{\rho} = \delta_{l,l'}\,. \tag{13}$$

The latter implies the following normalization condition for the expansion coefficients $C^{(l)}_{n,p}$:

$$\sum_{n',p';n,p} C^{(l)}_{n,p} C^{(l)}_{n',p'} \langle np|\mathcal{J}_\alpha(\rho,\theta)|n'p'\rangle = 1. \tag{14}$$

In the following, two different methods for calculating eigenvalues and eigenfunctions of Eq. (7) are presented, and their results analyzed.

III. ENERGY LEVELS AND WAVE FUNCTIONS

A. Exact diagonalization

The variational method is a powerful tool to solve the eigenvalue problem given by Eqs. (7) and (8). The coefficients $C^{(l)}_{n,p}$ (wave functions) and the corresponding eigenvalues can be obtained by direct substitution of expansion (12) into Eq. (7), yielding

$$\sum_{n,p} C^{(l)}_{n,p} f^0_{n,p}(\rho,\theta)\left(\mathcal{J}_\alpha(\rho,\theta) - \frac{(\mu^{(n)}_p)^2}{k^2}\right) = 0. \tag{15}$$

In matrix notation, the above equation can be cast as

$$[(\mathbf{k}^0)^{-1}\mathbf{J} - \gamma\mathbf{1}]\mathbf{C} = \mathbf{0}, \tag{16}$$

where $\gamma = 1/k^2$, $k^0_{s,s'} = (\mu^{(n)}_p)^2 \delta_{s,s'}$, $\mathbf{1}$ is the unit matrix, and $J_{s,s'} = \langle s|\mathcal{J}_\alpha(\rho,\theta)|s'\rangle$, where s represents the set of quantum numbers (n,p), taken in increasing order of $\mu^{(n)}_p$. The eigenvalues γ and eigenvectors $\mathbf{C}$ are then obtained from the secular equation

$$\det|(\mathbf{k}^0)^{-1}\mathbf{J} - \gamma\mathbf{1}| = 0. \tag{17}$$

To solve this equation we have used a numerical diagonalization procedure in a finite truncated basis of f^0_s. The first 11 energy levels E_l as a function of b/a obtained from Eq. (17) are shown in Fig. 2(a). It can be seen that the energy increases with decreasing ratio b/a, an effect that is dictated by the fact that the transformation (6) is not area preserving [9], and due physically to a stronger confinement geometry.

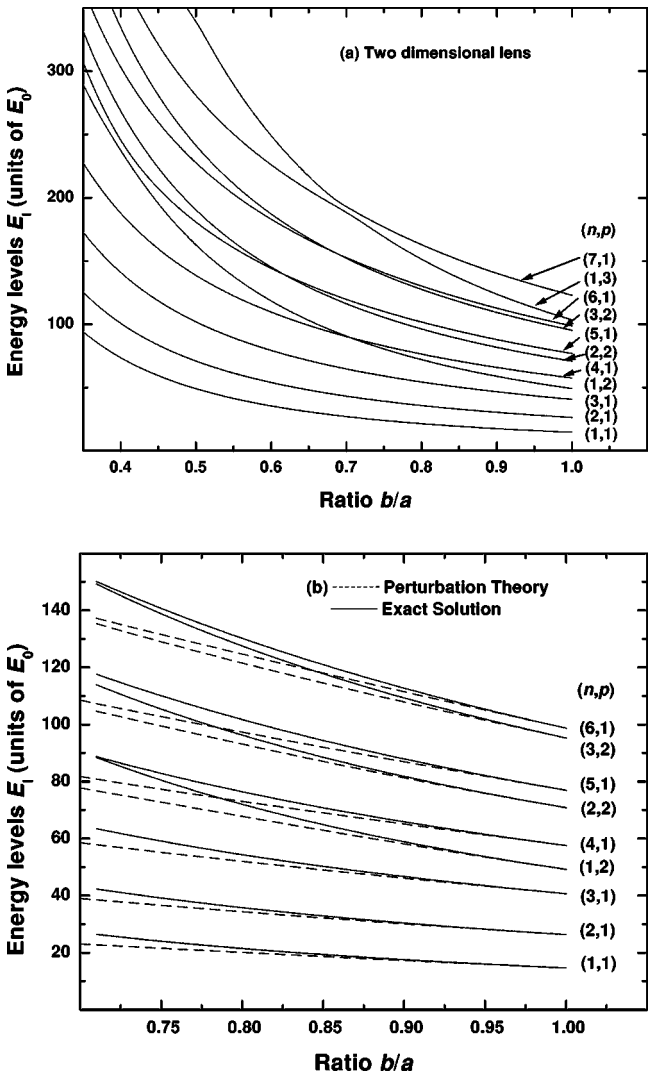

FIG. 2. (a) The first 11 energy levels E_l obtained from Eq. (17) as a function of the lens geometry parameter b/a. (b) Comparison between second order perturbation theory (dashed lines) and the variational method (solid lines), as a function of the ratio b/a. States are labeled at $b/a=1$ (semicircular boundary) by the quantum numbers (n,p).

It is possible to show that for small values of b/a the function $\langle s|\mathcal{J}_\alpha(\rho,\theta)|s'\rangle$ is proportional to $(b/a)^{-2}$.

An important aspect that must be taken into account is the symmetry of the equation of motion (16). The matrix $\langle s|\mathcal{J}_\alpha(\rho,\theta)|s'\rangle$ couples states fulfilling the selection rule $|n-n'|=$ even number. Hence, the symmetry present in the operator (7) allows the separation of the eigenfunctions into two Hilbert subspaces, which we will denote by S and A. The full Hilbert space is a combination of even (n-odd) and odd (n-even) functions for the subspaces S and A, respectively. As the given symmetry remains valid for any b/a value, we will label the states for $b/a<1$ with the same quantum numbers (n,p) as we use for $b=a$. In Fig. 2(a) we see clearly the level crossing between states with the different symmetries S and A. An example of such a crossing is found at $b/a\approx 0.7$, where the levels (1,2) and (4,1) fully cross. On the other hand, nearby levels belonging to the *same* Hilbert subspace

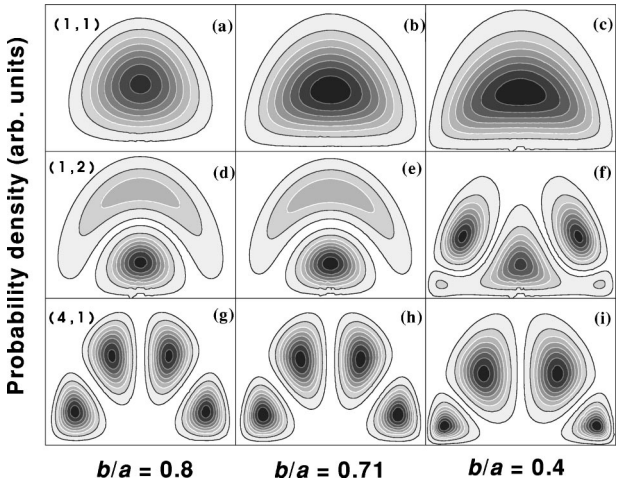

FIG. 3. Contour plots of the probability density $|F_l|^2$ for (1,1), (1,2), and (4,1) states and different values of the b/a ratio. The darker filling color indicates stronger spatial localization of the state. Size of lens has been rescaled in all panels.

present an anticrossing at certain values of b/a, as observed between the levels (1,2) and (5,1) at $b/a \approx 0.4$, and more clearly between levels (1,3) and (7,1) at $b/a \approx 0.7$. One should notice that the results presented have been achieved using matrices of size at least 600×600 and typically larger. The results are fully converged to high numerical accuracy.

Figure 3 shows contour plots for the probability density $|F_l|^2$ for different energy levels and b/a values. In Figs. 3(a)–3(c) the ground state (1,1) extends increasingly over the entire domain as the ratio b/a decreases. Figures 3(d)–3(f), on the other hand, represent the contour plots for the state labeled with quantum numbers (1,2) at $b/a=1$. Similarly, Figs. 3(g)–3(i) correspond to the energy level with labels (4,1) at $b/a=1$. In Figs. 3(d)–3(f) we see that the ''flatter'' lens geometry has a stronger effect on the probability density $|F_l|^2$ for the (1,2) level, provoking its rapid variation as a function of the decreasing ratio b/a. Otherwise, as shown in Figs. 3(g)–3(i), a smooth dependence on the b/a ratio is observed for the $|F_l|^2$ function of some states, such as (4,1) shown here. This different behavior is explained by its energy dependence [see Fig. 2(a)], as the state (1,2) goes higher in energy than (4,1) and experiences a stronger repulsion from the boundary surface defining the lens. This stronger repulsion results in the nodal structure shown in Fig. 3(f).

B. Perturbation theory

The coefficients $C_{n,p}^{(l)}$ in Eq. (12) and the eigenvalues $\overline{k^2}$ can be obtained by perturbation theory if $b \approx a$, i.e., $\alpha \to 1$. In this case, the 2D lens represents a perturbation from the semicircular geometry. In other words, the operator (7) can be rewritten in the form

$$(H_o + H_p)F(u,v) = 0, \tag{18}$$

with

$$H_o(u,v) = \nabla^2_{(u,v)} + \overline{k^2}, \tag{19}$$

$$H_p(u,v) = \overline{k^2}[\mathcal{J}_\alpha(u,v) - 1], \tag{20}$$

where the operator H_p vanishes when $\alpha \to 1$ and can be considered as a small perturbation operator. In order to find the solution of Eq. (18) as a function of the perturbation H_p, we use a modified Rayleigh-Schrödinger perturbation theory. We note that the operator H_p depends on the eigenvalue $\overline{k^2}$, and as such requires a somewhat different approach from the typical perturbation method used in quantum mechanics. Substituting Eq. (12) in Eq. (18) we get

$$[(\overline{k^2} - k_o^2) + \langle s|H_p(\overline{k^2})|s\rangle]C_s^{(l)} + \sum_{s' \neq s} \langle s|H_p(\overline{k^2})|s'\rangle C_{s'}^{(l)} = 0, \tag{21}$$

where we have used a unique quantum number s to label the (n,p) states as previously mentioned. We can represent the coefficients C_s and the eigenvalues $\overline{k^2}$ in a power series of the small parameter $\lambda = \mathcal{J}_\alpha - 1$. From Eq. (21) we obtain up to second order in λ that the eigenvalues $\overline{k^2}$ are given by

$$\overline{k_l^2} = (1 - \lambda_{l,l})(k_{l,l}^0)^2 + \frac{\lambda_{l,l}^2 (k_{l,l}^0)^2}{2} + \sum_{l' \neq l} \frac{(k_{l,l}^0)^2}{(k_{l,l}^0)^2 - (k_{l',l'}^0)^2} (\lambda_{l,l'})^2, \quad l = 1,2,\ldots, \tag{22}$$

and the wave functions up to first order are given by

$$F_l = f_l^0 - \frac{\lambda_{l,l}}{2} f_l^0 - \sum_{l' \neq l} \frac{(k_{l,l}^0)^2}{(k_{l,l}^0)^2 - (k_{l',l'}^0)^2} \lambda_{l,l'} f_{l'}^0, \tag{23}$$

where

$$\lambda_{l,l'} = \langle l|\mathcal{J}_\alpha(\rho,\theta) - 1|l'\rangle. \tag{24}$$

A comparison for the first nine energy levels between second order perturbation theory (dashed lines), as expressed in Eq. (22), and the exact solution (solid lines) is shown in Fig. 2(b). We can see an excellent agreement between the two methods for $b/a > 0.9$ (at least for these levels), while for the first three levels the agreement remains acceptable up to $b/a \approx 0.85$. It is clear that the perturbation $\mathcal{J}_\alpha - 1$ has more influence on the upper levels than in the lower ones, as one would anticipate, and that the perturbation due to the lens geometry is stronger as the ratio b/a decreases. For the wave functions calculated from Eq. (23), we find that the agreement with the exact solutions is excellent, exhibiting the same behavior as that discussed for the energy levels.

C. Onset of chaotic signatures

In Fig. 3 we should also notice the localization of all states toward the plane, leading to a strong change in the nodal structure of the wave function, as the ratio b/a decreases. The in-plane localization effect is highly correlated with the transition to chaos [9], as will be described below. Another aspect emerges from the energy spectrum as a strong signature of quantum chaos, i.e., the level repulsion or avoided crossing between levels with the same symmetry, as

was discussed previously. To clarify this behavior, we proceed with a study of the level spacing of the energy spectrum in terms of the ratio b/a. This analysis is commonly used to characterize the spectrum, and has been utilized as an indicator of chaotic behavior in a system [6,9,10]. We analyze the probability density $P(\nu)$ of finding an energy level (nearest-neighbor) spacing ν in a fixed interval $d\nu$, and normalized by

$$\int_0^{\nu_{max}} P(\nu)d\nu = 1, \tag{25}$$

where ν_{max} is the maximum level spacing and the variable ν in units of $E_0 = \hbar^2/(2ma^2)$ is given by

$$\nu_i = (E_i - E_{i-1})/E_0 . \tag{26}$$

Since we have to deal with a bounded and finite subset of the energy spectrum where the infinitesimal $d\nu$ becomes a discrete set of numbers, $d\nu \to \Delta\nu$, the distribution $P(\nu)$ needs to be represented by a histogram function $P(\Delta\nu)$. Although this has been the most commonly used procedure, we find it is preferable to compute the integrated or cumulative probability function [6,11]

$$I(\nu) = \int_0^{\nu} P(\nu')d\nu' . \tag{27}$$

The main advantage of working with Eq. (27) is that the function $I(\nu)$ does not depend on the specific binning used to create the histograms of $P(\Delta\nu)$. Either of these functions, $I(\nu)$ or $P(\nu)$, is compared with limiting distribution functions [12–16]. A typically used distribution is the Brody function [12]

$$P_\alpha(\nu) = (1+\alpha)\beta_\alpha \nu^\alpha \exp(-\beta_\alpha \nu^{\alpha+1}), \tag{28}$$

derived empirically to interpolate between the known limits studied in random matrix theory (RMT) by Wigner [6,17]. In Eq. (28), α is a phenomenological parameter, β is given by

$$\beta_\alpha = [\Gamma(1/(1+\alpha)+1)]^{1+\alpha}, \tag{29}$$

to provide proper normalization, and $\Gamma(x)$ is the Gamma function [18]. For $\alpha = 0$, $P_\alpha(\nu)$ is nothing but the Poisson distribution typical of classically integrable systems, while for $\alpha = 1$ it reduces to the Wigner distribution obtained from the Gaussian orthogonal ensembles of RMT [6,12]. In Fig. 4(a) the integrated probability function $I(\nu)$ is shown for the case of eigenstates with even symmetry, as a function of $\nu/\langle\nu\rangle$ for different values of the lens deformation parameter b/a, and where $\langle\nu\rangle$ is the mean level spacing. For the sake of comparison, the Poisson and Brody distributions are also shown.

As stated above, if we are dealing with a semicircular geometry ($b/a = 1$), the energy levels are given by the zeros of the Bessel function, and their spacing distribution function is well described by the Poisson distribution, as expected for an integrable system [9]. For $b/a = 0.8$ the system is no longer integrable and $I(\nu)$ can be fitted reasonably well by the distribution function (28), with $\alpha = 0.28$. For a flatter

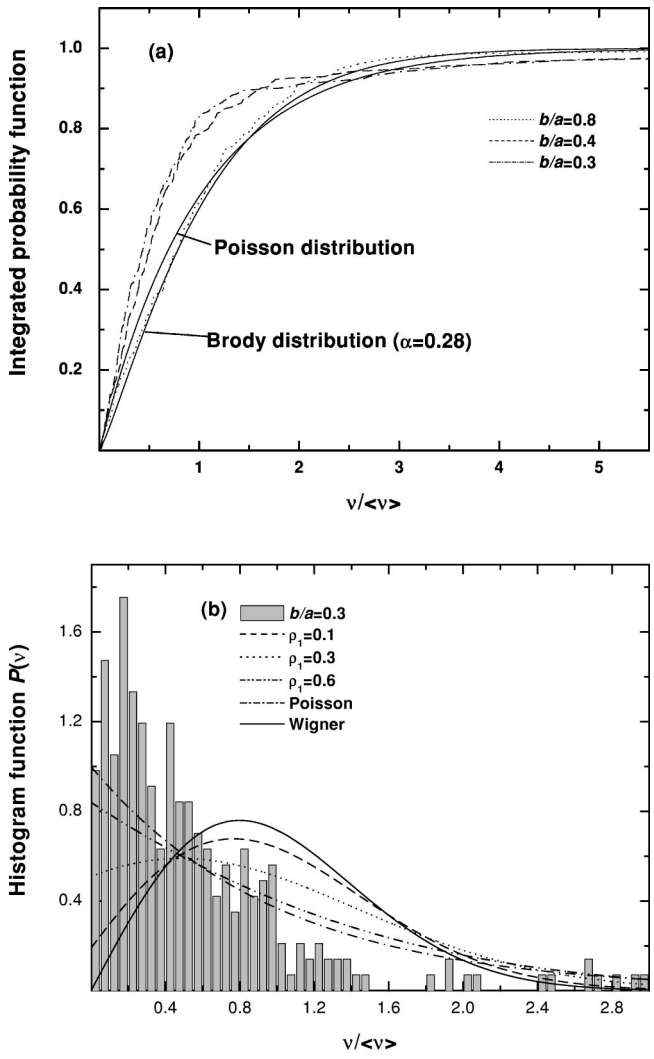

FIG. 4. (a) Integrated probability as a function of normalized level spacing for a cylindrical quantum lens and values of the ratio $b/a = 0.8$, 0.4, and 0.3. The Poisson and Brody distributions are also indicated. (b) Normalized level spacing histogram for $b/a = 0.3$. For comparison, the Berry-Robnik, Poisson, and Wigner functions are also plotted.

lens, $b/a = 0.7$ and lower, the integrated probability (27) clearly departs from the monotonic behavior predicted by the Brody distribution. This can be seen in Fig. 4(b) where the normalized level spacing histogram $P(\Delta\nu)$ for $b/a = 0.3$ is shown and the distribution obtained is obviously neither Poisson-like nor fully Wigner-like. As the b/a ratio decreases, a further spreading of the distribution function $P(\nu)$ is obtained, with a clear change in its characteristics. It is remarkable that $P(\nu = 0) \neq 0$ for strong deformations, $b/a \ll 1$, indicating the possibility of a mixed phase space (see below).

To further explore the properties of the spectrum, the normalized function $P(\Delta\nu)$ is also compared with the Berry-Robnik distribution (BRD) proposed for mixed phase space systems [13,16], and which for the particular case of a two-component phase space has the form

$$P_2(\nu,\rho_1)=\rho_1^2\exp(-\rho_1\nu)\operatorname{erfc}\left(\frac{\sqrt{\pi}}{2}\rho_2\nu\right)+\left(2\rho_1\rho_2+\frac{1}{2}\pi\rho_2^3\nu\right)\exp\left(-\rho_1\nu-\frac{1}{4}\pi\rho_2^2\nu^2\right), \quad (30)$$

where $\operatorname{erfc}(x)$ is the complementary error function and ρ_1 and ρ_2 are the Liouville measures for the regular and chaotic regions of the phase space on the Poincaré surface of section (PSOS), respectively. These parameters fulfill the condition

$$\rho_1+\rho_2=1, \quad (31)$$

since the phase space volume is preserved. In Fig. 4(b), the BRD function for several values of ρ_1 is shown. As can be seen, a certain degree of agreement is reached for $\rho_1=0.6$, mainly in the $\nu\approx 0$ region, since both P and P_2 are finite in this region. We should also comment that the integrated probability function $I_2(\nu)$ obtained from integrating the distribution $P_2(\nu,\rho_1)$ fits well the results of Fig. 4(a) (not shown) for $b/a=0.8$ with $\rho_1=0.6$, while poorer or no agreement is obtained for ratios b/a smaller than 0.7.

Similar results showing a strong departure from RMT have been reported in [19] for electrons interacting via a Coulomb potential in a semiconductor quantum dot in an external magnetic field. Although in many systems the $P_\alpha(\nu)$ distribution function is well described by the phenomenological power law of the Brody function, this is not always the appropriate description for all parameter values. The nature of the level repulsion due to the confinement of the lens geometry appears not to follow this simple interpolation scheme in general, especially as the ratio b/a decreases. However, the interpolation works quite well for the case of small deformations of the lens from the semispherical (-circular) shape, as can be seen in Fig. 4(a) for $b/a=0.8$; our calculations show that this behavior is indeed exhibited for both families of distributions considered, as long as $b/a>0.7$. In the case of strong departures from the semicircular geometry, a more complex description of the energy anticrossings is needed. Other phenomenological distribution functions have been proposed by Izrailev and by Casati *et al.* for the level spacing [20,21]. All of these have the form $P(\nu)\propto\nu^t$, where t is a model parameter. This does not agree with our results, since we have $P(\nu=0)\neq 0$. As reported in the literature, this more complex distribution is indicative of a mixed phase space, where different regions are classically integrable or quasiperiodic, while others are chaotic. This is the case of Fig. 4 for $b/a<1$ where the distribution would never reach $P(\nu=0)=0$, since the regular component has a nonzero probability for the $\nu\to 0$ spacing in agreement with the Berry-Robnik scenario [13,16]. In order to elucidate this behavior explicitly for different lens geometries, we analyze below the classical dynamics as b/a decreases from unity.

Figure 5 shows Poincaré sections (PSOS's) for the lens billiard in different projections. These plots are generated for 30 initial conditions near periodic orbits in the nondeformed geometry ($b/a=1$) with a constant velocity modulus; all trajectories are followed up for 5000 rebounds at the boundaries. As can be seen in Fig. 5(b) there is a clear regular motion for the semicircular lens geometry, while for a small

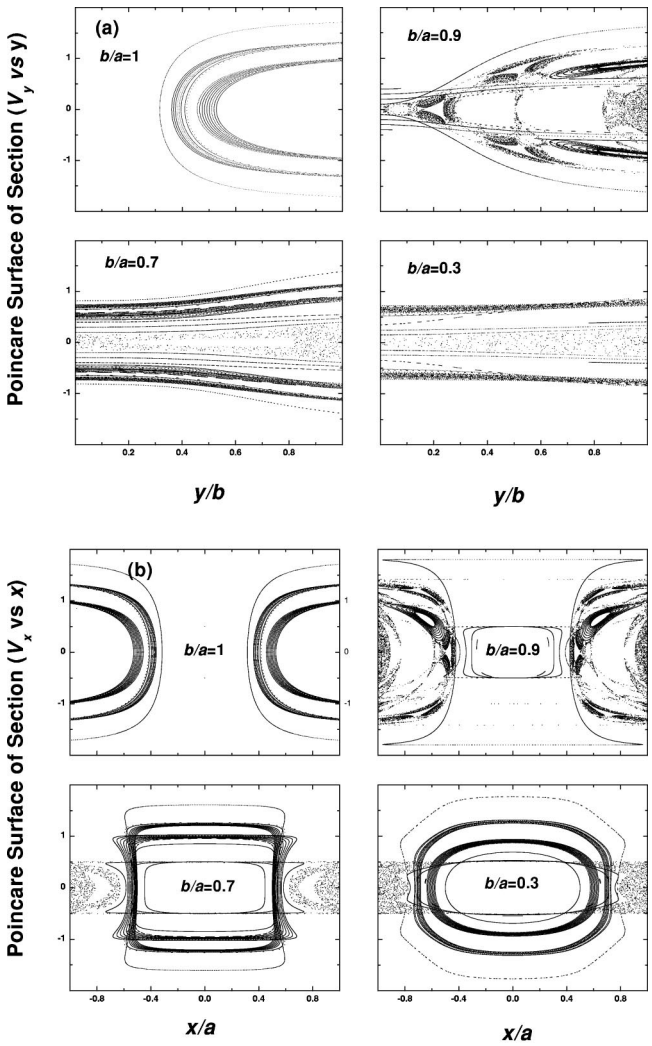

FIG. 5. (a) Poincaré surface of sections for a quantum lens billiard and values of the ratio $b/a=1$, 0.9, 0.7, and 0.3. (a) V_Y velocity component versus normalized length Y/b at $X=0$ and $V_X>0$. (b) V_X velocity component versus normalized length X/a at $Y=0$ and $V_Y>0$. The velocities are given in arbitrary units where $V_X^2+V_Y^2=2$.

deformation ($b/a=0.9$) a great deal of mixing already emerges. A lens strongly deformed ($b/a=0.3$), however, presents more of a regular pattern located mainly at the center, together with the chaotic region at $x/a\sim\pm 1$. In the case of the PSOS V_X vs X, Fig. 5(b), the picture is quite similar for small deformations but quite different for a flatter lens shape. Here, it is noted that for deformations as small as $b/a=0.7$ all the classical periodic orbits are broken and for extremely deformed lens geometries ($b/a=0.3$) wide chaotic zones appear. Nevertheless, it is clear that a great deal of complexity exists for $b/a<1$. The resulting mixed phase space was anticipated from the level spacing analysis in the quantum system above, and an estimate of the parameters in the BRD function is not far from $\rho_1\simeq 0.6$ for $b/a=0.8$. For smaller b/a values, however, the evaluation of ρ_1 is not as clear, and requires more detailed studies which we plan to present elsewhere. We should also mention, however, that

other systems with complex geometry do also exhibit mixed space behavior [22].

IV. CONCLUSIONS

We have formally obtained analytical solutions for the energy spectra and wave functions of a 2D or cylindrical lens geometry. The eigenenergies and eigenfunctions of a particle moving in this geometry are given in terms of the lens parameter b/a which characterizes the lens deformation with respect to the semicircular case. This set of lens-cap shapes represents stadia for the dynamics of mesoscopic electrons. We have also provided a complete set of orthogonal wave functions to describe a Dirichlet problem to characterize physical problems within the lens boundary, and it has been shown that the space of solutions is divided into two Hilbert subspaces with well-defined symmetry. We found that for small deformations ($b/a>0.9$) a modified Rayleigh-Schrödinger perturbation method provides accurate solutions for the lower eigenstates in the quantum lens. For smaller values of the ratio b/a, the eigenstates have to be described by the exact solution given by Eq. (16). The reported energies in units of E_0 [Fig. 2(a)] have a universal character in terms of the parameter b/a and, due to the breaking of circular symmetry by the lens deformation, the energy states of a given Hilbert subspace present anticrossings. In connection with this behavior, the probability density shows a tendency to localize the particle to the bottom region of the lens, and its nodal structure is strongly modified as the height of the lens decreases. A strong mixing of states occurs near anticrossing points, and the splitting increases as b/a decreases, while the system moves from fully integrable to a nonintegrable dynamical problem, i.e., to a quantum chaotic behavior in the sense of its level spacing statistics. In the case of semicircular geometry, the level spacing distribution is characterized by a Poisson distribution and follows the Brody function continuously for small lens deformations within the region $0.7<b/a<1$ (the exponential parameter α ranges between 0 and 0.28). We have found that the level spacing distribution departs more strongly from the Poisson and Wigner limits as the 2D lens becomes flatter, and the two-component Berry-Robnik distribution function or the phenomenological power law suggested in RMT fail to fully describe the level repulsion. This complex behavior of the level spacing distribution is characteristic of systems with classically mixed dynamics, and this is clearly the case for the lens, as shown in the Poincaré sections presented in Fig. 5. Notice that the appearance of quantum chaos in the quantum lens as a consequence of level anticrossing and the changing nodal structure of the wave functions is characterized by the single parameter b/a that measures the lens deformation.

ACKNOWLEDGMENTS

C.T.-H. would like to thank DAAD for the availability of computational facilities, and the financial support of the ''Cátedra de Ciencias Contemporánea'' at Jaime I University. S.E.U. acknowledges support from U.S. DOE Grant No. DE-FG02-91ER45334.

[1] A. MacKinnon, E. Castaño, and G. Kirczenow, in *Handbook on Semiconductors*, edited by P. T. Landsberg (North Holland, Amsterdam, 1992), Vol. 1, Chap. 16, pp. 863–975.
[2] P.M. Petroff and G. Medeiros-Ribero, MRS Bull. **21(4)**, 50 (1996); G.S. Solomon, J.A. Trezza, A.F. Marshall, and J.S. Harris, Jr., Phys. Rev. Lett. **76**, 952 (1996).
[3] See, for example, L. Gonzalez, J.M. Garcia, R. Garcia, F. Briones, J. Martinez-Pastor, and C. Ballesteros, Appl. Phys. Lett. **76**, 1104 (2000).
[4] J.J. Heremans, S. von Molnar, D.D. Awschalom, and A.C. Gossard, Appl. Phys. Lett. **74**, 9 (1999), and references therein.
[5] C.M. Marcus, A.J. Rimberg, R.M. Westervelt, P.F. Hopkins, and A.C. Gossard, Phys. Rev. Lett. **69**, 506 (1992); A.M. Chang, H.U. Baranger, L.N. Pfeiffer, and K.W. West, *ibid.* **73**, 2111 (1994); J.P. Bird, K. Ishibashi, Y. Aoyagi, T. Sugano, and Y. Ochiai, Phys. Rev. B **50**, 18 678 (1994).
[6] M. C. Gutzwiller, *Chaos in Classical and Quantum Mechanics* (Springer, New York, 1990).
[7] P.M. Morse and H. Feshbach, *Methods of Theoretical Physics* (McGraw-Hill, New York, 1953).
[8] S.G. Mikhlin, *Variational Methods in Mathematical Physics*, Vol. 50 of International Series of Monographs in Pure and Applied Mathematics (Pergamon Press, Oxford, 1964).
[9] M. Robnik, J. Phys. A **17**, 1049 (1984).
[10] M.T. Lopez-Arias, V.R. Manfredi, and L. Salasnich, Nuovo Cimento Riv. **17**, 1 (1994).
[11] R. Badrinayaranan, J.V. Jose, and G. Chu, Physica D **83**, 1 (1994).
[12] T.A. Brody, J. Flores, J.B. French, P.A. Mello, A. Pandey, and S.S.M. Wong, Rev. Mod. Phys. **53**, 385 (1981).
[13] M.V. Berry and M. Robnik, J. Phys. A **17**, 2413 (1984).
[14] G. Lenz and F. Haake, Phys. Rev. Lett. **67**, 1 (1991).
[15] V. Lopac, S. Brant, and V. Paar, Z. Phys. A **356**, 113 (1996).
[16] M. Robnik, Nonlinear Phenom. Complex Syst. **1**, 1 (1984).
[17] E. Wigner, SIAM Rev. **9**, 1 (1967).
[18] *Handbook of Mathematical Functions*, edited by M. A. Abramowitz and I. Stegun (Dover, New York, 1970).
[19] S.E. Ulloa and D. Pfannkuche, Superlattices Microstruct. **21**, 21 (1997).
[20] F.M. Izrailev, Phys. Rev. Lett. **56**, 541 (1986).
[21] G. Casati, F.M. Izrailev, and L. Molinari, J. Phys. A **24**, 4755 (1991).
[22] L. Meza-Montes and S.E. Ulloa, Phys. Rev. E **55**, 6319 (1997).